Anisotropic Kepler problem in a non–rotationally-symmetric Eaton lens

Tao Hou and Huanyang Chen*
Department of Physics, Xiamen University, Xiamen 361005, China

(Received 27 September 2021; accepted 1 March 2022; published 4 April 2022)

In this paper, we prove that the anisotropic Kepler problem in two-body motion can be analogous to optical non–rotationally-symmetric Eaton lens. According to the numerical calculation and simulation results, when the mass ratio of anisotropic Kepler problem $\mu > 1$, the corresponding non–rotationally-symmetric Eaton lens can simulate and reproduce the periodic orbits and chaotic characteristics of anisotropic Kepler problem in geometric optics and wave optics, respectively. In the extended study, when a beam is incident to the non–rotationally-symmetric Eaton lens from air, different from the light properties in traditional Eaton lens, the deflected beam is no longer along 180°, and may have scatterings in other directions, which are influenced by the incident direction and mass ratio μ. The results provide a successful reference for the analogy between optical and mechanical phenomena.

DOI: 10.1103/PhysRevA.105.043501

I. INTRODUCTION

The anisotropic Kepler problem (AKP) originally comes from quantum mechanics and it is a modified model of the Kepler problem. The model can be used to describe the motion of two bodies in the anisotropic configuration plane under the interaction of universal gravitation described by Newton's law of universal gravitation. It was first proposed by Gutzwiller [1] in 1973, who chose to study AKP because it was a chaotic system, i.e., one without stable periodic orbits. It was widely disseminated and considered one of the most suitable models for studying the physics of semiconductors. The dynamics of each system will be very irregular when the masses are not equal in each direction of the Hamiltonian. Gutzwiller [2] subsequently proved a one-to-one correspondence between a set of trajectories of two-dimensional AKP and binary Bernoulli sequences, which indicated that the system has strong chaotic characteristics. Later, Broucke [3] changed the form of Hamiltonian in AKP, and found two periodic orbits of stability with the periods of 3 and 5, respectively, under the condition that the mass ratio μ was approximately equal to 1.5. However, since periodic orbits disappear when the μ is greater than 1.748, Gutzwiller [4] believed that when μ is greater than 2, particles do not have stable periodic orbits and chaos always exists. Bai [5] also thought AKP is chaotic even for mass ratio μ slightly larger than 1 because the perturbation would be very large when a particle approached the origin. Contopoulos [6] also obtained a similar conclusion by the calculation results that the Lyapunov feature number of chaotic orbits were positive for various values of μ. In a follow-up study, Arribas [7] proved the nonintegrability of planar and spatial anisotropy Kepler problems by analyzing the properties of differential Galois groups of variational equations around some particular solutions. Abouelmagd [8] proved that the Kepler problem with weak anisotropy has two periodic orbits at each energy level, and both of them bifurcated from the elliptical orbit of the Kepler problem with high eccentricity. Anisotropic mass tensor and interactions with gravity are common. For example, the planar isosceles three-body problem, which can be reduced to a natural Hamiltonian system [9,10], corresponds to an anisotropic Kepler potential with two degrees of freedom, standard kinetic energy, and additional radial terms. At the same time, the rhombic charged tetrahedron problem [11] also involves the AKP. Maciejewski [12] also proposed that the anisotropic Kepler system can be realized through a two-point mass system which move in perpendicular lines (or planes). Therefore, it also reveals the possibility that AKP can be realized in other fields.

The mechanical equation is very similar to the optical wave equation. When the mass (potential) and refractive index satisfy certain conditions, optics can correspond with theoretical mechanics by analogy. The remarkable similarity between the two disciplines can be demonstrated by matter wave cloaking [13] and electromagnetic cloaking [14] based on transformed coordinates. The conformal cloak for waves [15] based on the Hooke and Kepler potentials also reveals that the intersection of mechanics and optics can produce more magical phenomena. AKP, considered as the suitable model for studying the hard chaos, introduces anisotropic mass and non–rotationally-symmetric potential, which corresponds to the new optical refractive index and generates new phenomena that have not been considered before.

There are many lenses with different functions in the optics field. Their refractive index distribution can be divided into two types: isotropic and anisotropic, and isotropic refractive index lenses are mostly studied. Among them are a special kind of isotropic lenses, known as absolute instruments for their perfect imaging performance in geometric optics [16–20]. The most famous absolute instruments are Luneburg lens [21], Eaton lens [22,23], and Maxwell fisheye lens [24,25]. Although the basic refractive index of traditional

*kenyon@xmu.edu.cn

absolute lenses all have rotation symmetry, recent studies have shown that when Luneburg lens breaks rotation symmetry [26,27], Lissajous lens [26] or new Luneburg-Lissajous lens [27] can still perform imaging or self-imaging under some conditions, resulting in many interesting phenomena. Traditional Eaton lens has excellent self-focusing properties, in which light propagates in perfect circles or ellipses. It can be applied in a wide range, such as super-resolution imaging [28], photonic crystal [29], and geodesic lens [30,31] to achieve curved imaging.

In this paper, we find that the Schrödinger equation of the Kepler potential is in agreement with the wave equation of light in Eaton lens. In addition, when the rotation symmetry of the Eaton lens is broken, the ray propagation trajectory is equivalent to the particle's trajectory of AKP after coordinate transformation. Therefore, we observe light fields and behaviors of rays with different μ in wave optics and geometric optics. The results show that as μ increases, the non–rotationally-symmetric Eaton lens (NSEL) loses its self-focusing property, and the periodic orbits and chaos in AKP can be found in the light fields and ray behaviors. In addition, when a beam is incident into the NSEL from air, with the increase of μ, the deflected angle of the beam incident from the left side gradually increases, and strong scattering will occur, while the deflected angle of the beam incident from the upper side becomes smaller, and there is little scattering. The results in the paper includes the analytical solutions calculated by our theory and the simulation results from commercial finite-element solver COMSOL MULTIPHYSICS.

II. THEORY

Initially, Gutzwiller [1] proposed the Hamiltonian in AKP:

$$H = \frac{p_1^2}{2m_1} + \frac{p_2^2 + p_3^2}{2m_2} - \frac{e^2}{\kappa\sqrt{q_1^2 + q_2^2 + q_3^2}}. \tag{1}$$

The original AKP was used to describe the gravitational effects of surrounding lattices on the nucleus charge in Si and Ge, where κ is dielectric constant of the lattices, e is electric charge, q_β and p_β $(\beta = 1, 2, 3)$ are the coordinates and momenta of the particles on different axes, respectively. The masses in different direction (m_1, m_2) are not equal, which is the significant difference between the ordinary Kepler problem and anisotropic Kepler problem.

In Cartesian coordinates, the normalized Hamiltonian $(\kappa = e = 1)$ becomes

$$H_G = \frac{1}{2}\left(\frac{U_G^2}{\mu_G} + \frac{V_G^2 + W_G^2}{v_G}\right) - \frac{1}{\sqrt{x_G^2 + y_G^2 + z_G^2}}. \tag{2}$$

Consider its representation in two dimensions, i.e.,

$$H_G = \frac{1}{2}\left(\frac{U_G^2}{\mu_G} + \frac{V_G^2}{v_G}\right) - \frac{1}{\sqrt{x_G^2 + y_G^2}}. \tag{3}$$

Here x_G and y_G are the normalized Cartesian coordinates, $U_G = \mu_G \dot{x}_G, V_G = v_G \dot{y}_G$ are the momentum. Among them, μ_G and v_G correspond to the m_1 and m_2, respectively, and $\mu_G v_G = 1$. In this case, $\mu_G > 1$, i.e., the x axis is along the heavy direction of mass μ_G. Hence, the mass ratio of the particle is defined as $\mu = \frac{\mu_G}{v_G} = \mu_G^2$. In a way similar to Gutzwiller [4], the eigenvalue of H_G is $-1/2$.

Broucke [3] uses coordinate transformation

$$x_B = {\mu_G}^{2/3} x_G, \quad y_B = {\mu_G}^{-1/3} y_G \tag{4}$$

to reduce the mass factor under momentum, and get a new Hamiltonian:

$$H_B = \frac{1}{2}\left(U_B^2 + V_B^2\right) - \frac{1}{\sqrt{\mu_B x_B^2 + y_B^2}}, \tag{5}$$

where

$$H_B = {\mu_G}^{1/3} H_G, \tag{6}$$

$$\mu_B = {\mu_G}^{-2}. \tag{7}$$

The basic difference between these two Hamiltonian expressions is that anisotropy of Eq. (2) is introduced in the kinetic energy of the Hamiltonian, while anisotropy of Eq. (5) is introduced in the potential of the Hamiltonian.

The mechanical expressions of the Hamiltonian equation are

$$\frac{d\boldsymbol{r}}{dt} = \frac{\partial H}{\partial \boldsymbol{p}}, \quad \frac{d\boldsymbol{p}}{dt} = -\frac{\partial H}{\partial \boldsymbol{r}}, \tag{8}$$

where $\boldsymbol{r}$ and $\boldsymbol{p}$ are position and momentum in Hamiltonian, respectively. Substituting Eq. (5) into Eq. (8) in the Cartesian coordinate system, we get

$$\dot{x}_B = U_B, \quad \dot{y}_B = V_B, \quad \dot{U}_B = \frac{-\mu_B x_B}{\left(\mu_B x_B^2 + y_B^2\right)^{3/2}},$$
$$\dot{V}_B = \frac{-y_B}{\left(\mu_B x_B^2 + y_B^2\right)^{3/2}}. \tag{9}$$

The trajectories of particles can be obtained by solving the differential equations.

In optics for transverse electric (TE) mode, the electric field points in the vertical direction (orthogonal to the plane). If a planar medium with a two-dimensional gradient refractive index $n(x, y)$ is considered, its propagation process conforms to the Helmholtz equation:

$$\left(\nabla_x^2 + \nabla_y^2 + n^2 k_0^2\right)\psi = 0. \tag{10}$$

It can be found that the optical propagation equation in real space is very similar to the steady-state Schrödinger equation in mechanics:

$$\left(\nabla_x^2 + \nabla_y^2 + \frac{2m}{\hbar^2}(E - E_p)\right) \quad \psi = 0, \tag{11}$$

where E_p represents potential, E represents energy, and m represents the mass of the particle. In combination with Eqs. (5) and (11), we can obtain

$$\left(\nabla_x^2 + \nabla_y^2 + \frac{2}{\hbar^2}\left(\frac{1}{\sqrt{\mu_B x_B^2 + y_B^2}} - \frac{{\mu_B}^{-1/6}}{2}\right)\right)\psi = 0. \tag{12}$$

Here we set $\hbar = 1$, $k_0 = 1$. By comparing Eqs. (10) and (12), we can obtain the optical refractive index corresponding

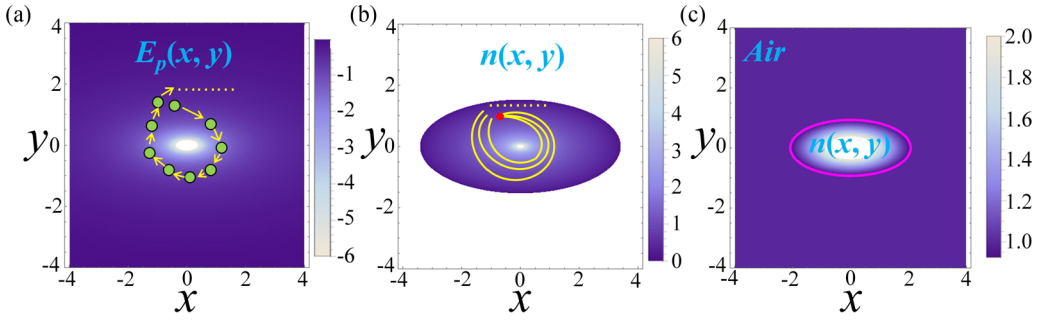

FIG. 1. (a) The cross section of the potential $E_p\,(x, y)$ in AKP. The green circles and yellow arrows around the center represent the particles and the direction of motion, respectively. (b) The elliptic cross section of the optical index $n(x, y)$ in NSEL. The red (upper) circle and yellow lines around the center represent the light source and the ray trajectory, respectively. The trajectories in the two system are unclosed and chaotic. (c) The schematic of the optical NSEL under the background of air. The pink ellipse around the center represents the boundary between NSEL and air. The units of *y*-*x* coordinate axes are set as m.

to AKP:

$$n(x, y) = \sqrt{\frac{2}{\sqrt{\mu_B x_B^2 + y_B^2}} - \mu_B{}^{-1/6}}. \tag{13}$$

It can be found that different energy levels of AKP correspond to different refractive indexes.

When $\mu_B = 1$,

$$n(x, y) = \sqrt{\frac{2}{\sqrt{x_B^2 + y_B^2}} - 1}, \tag{14}$$

which is exactly the refractive index distribution of traditional Eaton lens, verifying the correspondence between the isotropic Kepler problem and the optical Eaton lens. Hence, when $\mu_B \neq 1$, AKP corresponds to the refractive index of NSEL.

Similarly, the path of light rays can be determined by optical Hamiltonian equations,

$$\frac{d\boldsymbol{r}}{dt} = \frac{\partial\omega}{\partial\boldsymbol{k}}, \quad \frac{d\boldsymbol{k}}{dt} = -\frac{\partial\omega}{\partial\boldsymbol{r}}. \tag{15}$$

where $\boldsymbol{k} = n(x, y)\boldsymbol{k}_0$ is the wave vector of the ray and $\omega = \frac{c}{n(x,y)}k$ is the angular frequency in optics.

Expanding Eq. (15), we can get

$$\begin{aligned}
\frac{dx}{dt} &= \frac{\partial\omega}{\partial k_x} = \frac{ck_x}{nk} \\
\frac{dy}{dt} &= \frac{\partial\omega}{\partial k_y} = \frac{ck_y}{nk} \\
\frac{dk_x}{dt} &= -\frac{\partial\omega}{\partial x} = \frac{ck}{n^2}\frac{\partial n}{\partial x} = -\frac{ck\mu_B x(\mu_B x^2 + y^2)^{-(3/4)}}{\left(2 - \mu_B^{-1/6}\sqrt{\mu_B x^2 + y^2}\right)^{3/2}} \\
\frac{dk_y}{dt} &= -\frac{\partial\omega}{\partial y} = \frac{ck}{n^2}\frac{\partial n}{\partial x} = -\frac{cky(\mu_B x^2 + y^2)^{-(3/4)}}{\left(2 - \mu_B^{-1/6}\sqrt{\mu_B x^2 + y^2}\right)^{3/2}}.
\end{aligned} \tag{16}$$

The ray trajectories can be obtained by solving the differential equations.

It is worth noting that in the mechanical definition, for a particle at position $\boldsymbol{r}$, momentum $\boldsymbol{p} = \hbar\boldsymbol{k}$ and Hamiltonian $H = \hbar\omega$. In order for the solutions of the two equations to be equivalent, the initial momentum of the particle needs to satisfy $|\boldsymbol{p}| = |\sqrt{U_B{}^2 + V_B{}^2}| = |\boldsymbol{k}| = |n|$. According to Eqs. (10) and (11), the energy E of the mechanical AKP affects the optical refractive index n, and the value of n also affects the initial momentum of anisotropic particles corresponding to the light rays. So, the difference of the energy level influences the correspondence between the momentum of particles and the wave vectors of rays.

III. RESULTS

In order to verify the relationship between the particle trajectory in AKP and the ray trajectory in the NSEL, we set a simple model as shown in Fig. 1 and select the same mass ratio and initial motion parameters.

First of all, in the AKP, we choose a classic example of mass ratio $\mu = 5$ (μ_B= 0.2) in Gutzwiller's book [4], so the potential of the particles $E_p = -\frac{1}{\sqrt{0.2x_B^2 + y_B^2}}$. The initial values of position and momentum are set as $x_B[0] = 1.4$ m, $y_B[0] = 0.627$ m, $U_B[0] = -0.72$ m/ns, and $V_B[0] = -0.65$ m/ns . The analytical results of the particles' trajectories calculated by Eq. (9) at times t = 0–25 (ns) and t = 25–35 (ns) are shown in Figs. 2(a) and 2(d), respectively. When t is small, the particle exhibits stability under the interaction of gravity and moves along periodic orbits. When t increases gradually, the chaos of particle is gradually reflected, and the trajectory begins to be disordered. This is because when the mass ratio is greater than 2, the periodic orbits of the particles will be destroyed with the increase of time, resulting in hard chaos [4].

Similarly, when the mass ratio $\mu = 5$, the refractive index of the corresponding NSEL is $n(x, y) = \sqrt{\frac{2}{\sqrt{0.2x_B^2 + y_B^2}} - 5^{1/6}}$, and the initial incident conditions are set as same as those of the moving particles $x_B[0] = 1.4$ m, $y_B[0] = 0.627$ m, $k_x[0] = -0.72$ m^{-1}, and $k_y[0] = -0.65$ m^{-1} . The analytical solutions calculated by Eq. (16) and simulation results of ray trajectory at the different times are shown in Figs. 2(b), 2(c), and 2(d). By comparing the mechanical trajectory and the ray trajectory, it can be found that when t is small, the motion trajectory of the particles is completely consistent with the ray trajectory in the light propagation, which verifies the commonality of AKP and NSEL theory. When t gradually

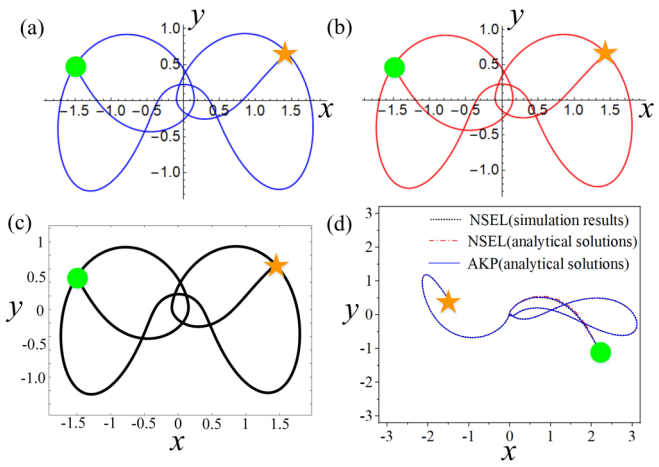

FIG. 2. (a) The analytical results of particles' trajectories at $t = 0$–25 ns in AKP. The initial values of motion are set as $x_B[0] = 1.4$ m, $y_B[0] = 0.627$ m, $U_B[0] = -0.72$ m/ns, and $V_B[0] = -0.65$ m/ns. (b) The analytical solutions and (c) simulation results at $t = 0$–25 ns of ray trajectories in NSEL. The initial incident conditions are set the same as those of the moving particles:$x_B[0] = 1.4$ m, $y_B[0] = 0.627$ m, $k_x[0] = -0.72$ m^{-1}, and $k_y[0] = -0.65$ m^{-1} (d) The particles' trajectories in AKP and ray trajectories in NSEL at $t = 25$–35 ns. The units of y-x coordinate axes are set as m. The orange stars and green circles in all subgraphs represent initial positions and end positions of trajectories, respectively.

increases, influenced by chaos, particles and light rays will no longer follow periodic trajectories. In addition, there are slight differences among the simulation results of AKP, analytical solutions, and simulation results of NSEL because of the weak precision errors of software or calculations, which can be seen in Fig. 2(d). All in all, we can further simulate the motion phenomena and laws in classical AKP by NSEL.

It is well known that light in Eaton lenses has the property of self-focusing [19], which corresponds to the closed-trajectory property of Kepler's problem. Periodic orbits and chaos in AKP must correspond to the peculiar properties of NSEL. In order to better explore the relevant laws, we introduced the Poincaré cross section in AKP for observation. The points of $y = 0$ m and $v > 0$ m/ns in the AKP trajectory corresponding to the NSEL are selected as the intercept points on the Poincaré cross section. When there is only one fixed point or a few solitary points on the Poincaré cross section, the trajectory is periodic; when there is a closed curve in the Poincaré section, the trajectory is quasiperiodic; The trajectory is thought as chaos when the Poincaré section consists of patches of dense points with fractal structure. Similar to Gutzwiller [4], we define $X = x(1 + \frac{U_B^2}{\mu_B})$, $U = \frac{2}{\pi}\tan^{-1}(\frac{U_B^2}{\sqrt{\mu_B}})$ as the horizontal and vertical coordinates of Poincaré cross section, respectively. In order to make equivalent the effect of point source for wave optics (a line current source) by geometrical optics, we select some special and representative incident directions as reference when calculating geometric optical trajectory and Poincaré cross section. In the computational simulation, the point sources are placed at (−1.5 m, 0) and (0, 1.5 m), respectively, and μ are set as 1, 1.1, 1.2, and 2 ($\mu_B = 1$, 0.91, 0.833 333, and 0.5). Different from the ray trajectory calculation, we add perfect matching layers on the boundary of the wave optical simulation regions. The simulation results of wave optics, geometric optics, and analytical solutions of Poincaré cross section are shown in Figs. 3 and 4.

In Fig. 3, the point source is placed on the left side. When $\mu = 1$, the point source will form as self-focusing, and the trajectories present ellipses, and only a few solitary points exist in the corresponding Poincaré cross section. When μ is slightly greater than 1 (taking $\mu = 1.1$ as an example), the rays are no longer along closed elliptic trajectories and do not pass through the other side of the lens. The Poincaré intercept points corresponding to the trajectories are evenly distributed on both sides of the y axis and form some closed curve (stability island from family 3 [6]). The light rays bifurcated from the elliptical orbits of the traditional Eaton lens, which can be considered as quasiperiodic orbits with stability, and there is slight scattering on the electric field. When μ gradually increases (taking $\mu = 1.2$ as an example), the light field and rays of the left side and right side are approximately symmetrically distributed, that is, the light from one side will reach the other side. At this time, there are dense spots on the Poincaré cross section while retaining the original island of stability. When μ is large (taking $\mu = 2$ as an example), both the light field and the rays are very chaotic, and the stability islands in Poincaré cross section constantly break up and change into hyperbolic dense points.

As shown in Fig. 4, the point source is placed on the upper side. When $\mu = 1$, the point source has the same self-focusing effect as Fig. 3. There are only a few solitary points in the corresponding Poincaré cross section. When μ is slightly greater than 1 (taking $\mu = 1.1$ as an example), the ray trajectories are still quasiperiodic orbits with certain stability. But, different from Fig. 3(h), the Poincaré intercepts are symmetric along the origin and make up different stable islands. When μ continues to increase (taking $\mu = 1.2$ as an example), although there are different degrees of scatterings in other directions, most of the electric field is distributed on the upper side. At this time, the Poincaré cross section adds many dense points while preserving the original island of stability. When μ becomes large (taking $\mu = 2$ as an example), the electric field and rays are very chaotic, but most of them still distribute on the upper side. The stability islands constantly split into hyperbolic dense points, showing chaotic characteristics.

In traditional Eaton lens ($\mu = 1$), the ray will follow an elliptical trajectory. After the ray incidents from the point (−1.5 m, 0), it will travel half the ellipse and undergo a sudden change of direction ($k_x > 0$ to $k_x < 0$) as it arrives at the x axis ($y = 0$) again. Similarly, after the ray incidents from the point (0, 1.5 m), it also undergoes a sudden change of direction $k_y < 0$ to $k_y > 0$) as it arrives at the y axis ($x = 0$) again. Here we call the points with sudden change of direction mutational points. According to Eq. (16), when $x = 0$, the value of dk_y/dt is not influenced by μ_B. However, when $y = 0$, the value of dk_x/dt is almost linear with the value of μ_B. Compared with the same condition in traditional Eaton lens, there is a bigger change of direction at the mutational points of the ray incident from the point (−1.5 m, 0) than of the ray incident from the point (0, 1.5 m) in NSEL. Combining

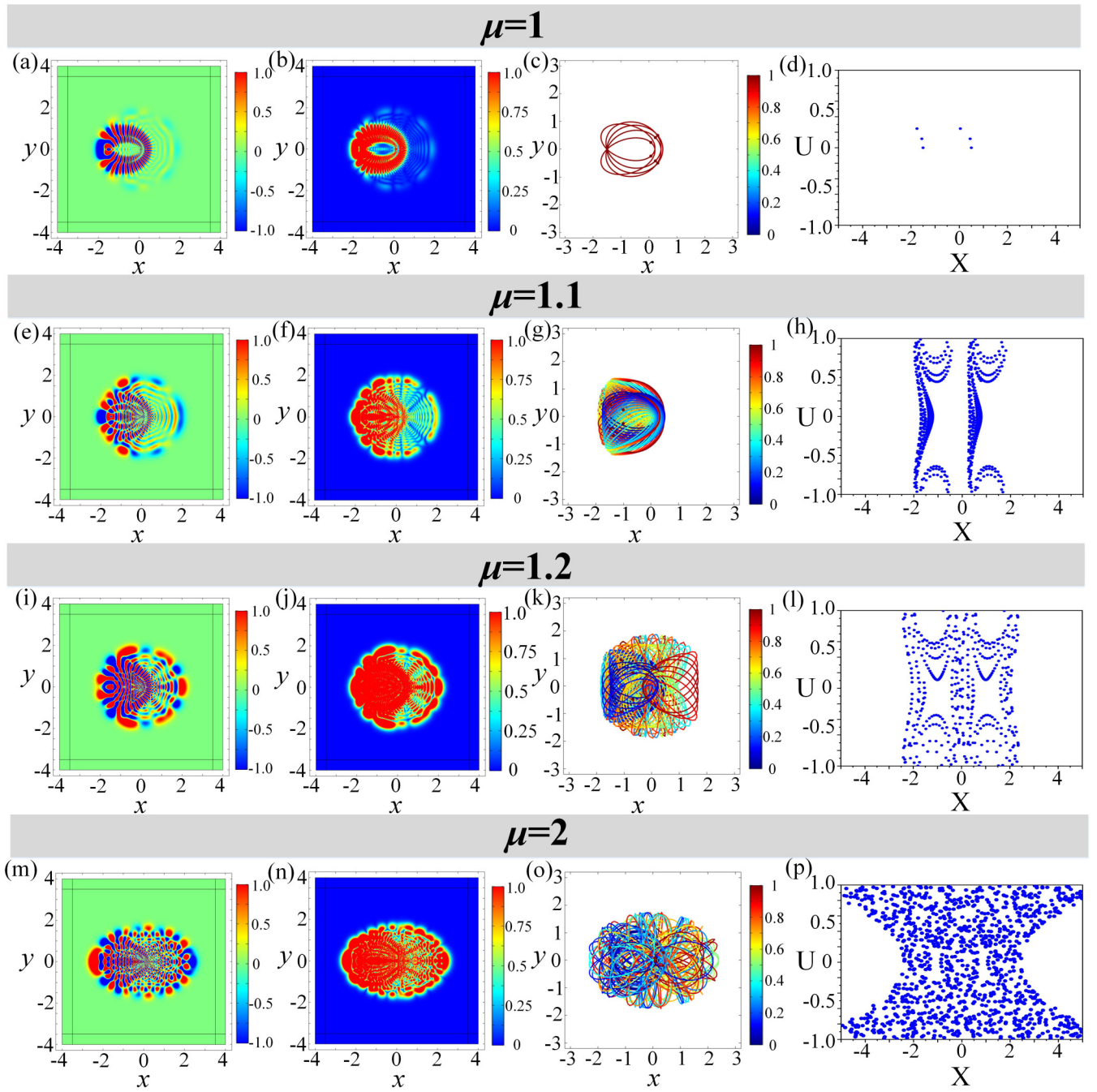

FIG. 3. The E_z component, the absolute value of the electric field, geometrical trajectories, and Poincaré cross section of different mass ration $\mu = 1$ (a)–(d); $\mu = 1.1$ (e)–(h); $\mu = 1.2$ (i)–(l); and $\mu = 2$ (m)–(p) when a point source is placed at $(-1.5\ \text{m}, 0)$. The horizontal and vertical coordinates of Poincaré cross section are set as $X = x(1 + \frac{U_B^2}{\mu_B})$, $U = \frac{2}{\pi}\tan^{-1}(\frac{U_B^2}{\sqrt{\mu_B}})$. The square boxes of subgraphs are simulation areas, and the layered boundaries in the first two columns of subgraphs are perfect matching layers. The units of y-x coordinate axes are set as m. The duration of geometric trajectory is set as $\Delta t = 600\,\text{ns}$.

the above discussion and the comparison between Fig. 3 and Fig. 4, we can find that the ray orbits from the top point (0, 1.5 m) are more stable than those from the left point $(-1.5\ \text{m}, 0)$.

Different from mechanics, in order to fit the actual experimental environment, the influence of air on the imaging effect of lens is often not negligible in the studying works of optical lens. Therefore, the refractive index $n(x, y)$ is set as Eq. (17) and the incident mode of light is changed from point source into beam.

$$n(x,y) = \begin{cases} 1 & (n < 1) \\ \sqrt{\frac{2}{\sqrt{\mu_B x_B^2 + y_B^2}} - \mu_B{}^{-1/6}} & (n \geqslant 1) \end{cases}. \tag{17}$$

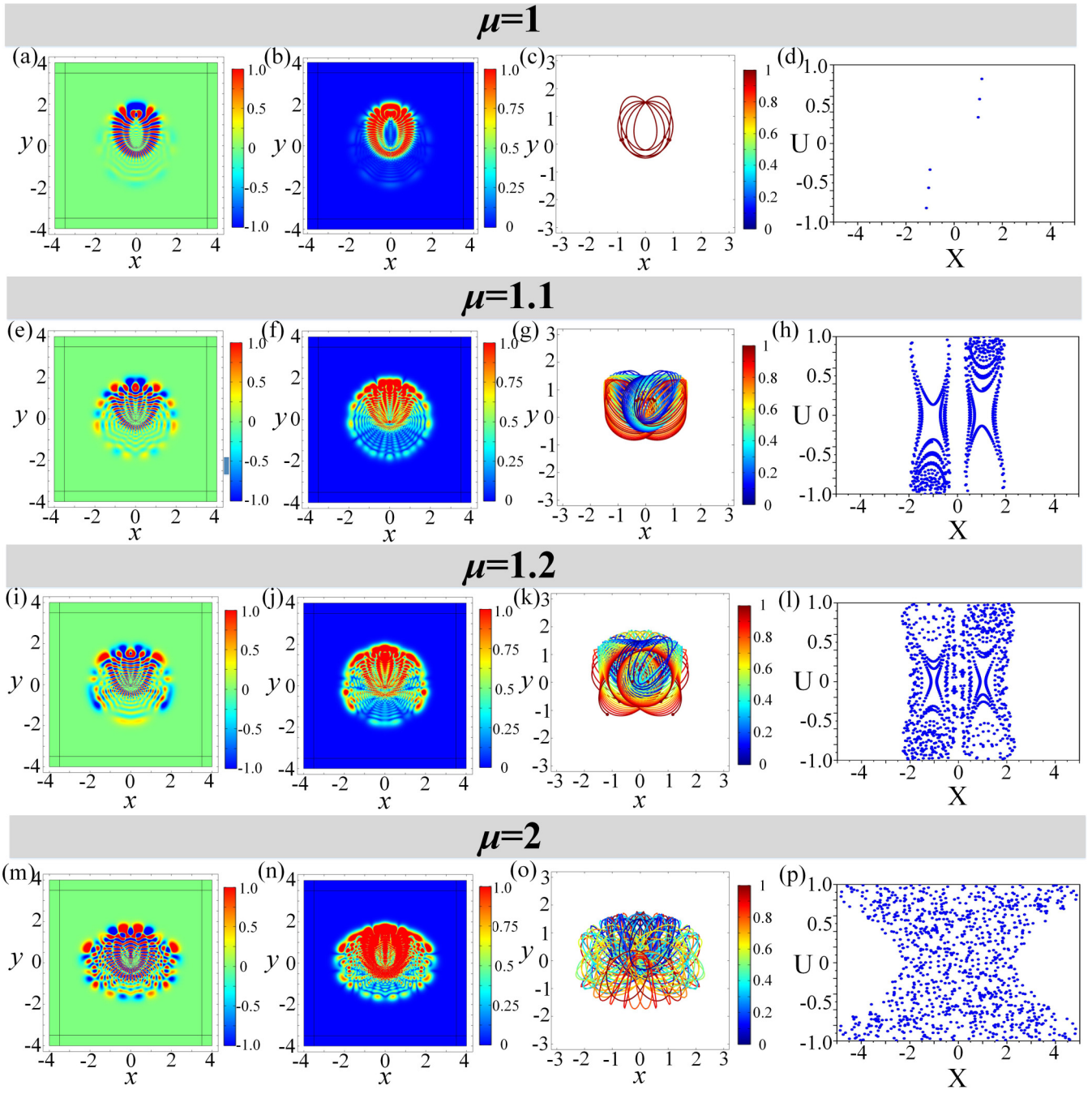

FIG. 4. The E_z component, the absolute value of the electric field, geometrical trajectories, and Poincaré cross section of different mass ration $\mu = 1$ (a)–(d); $\mu = 1.1$ (e)–(h); $\mu = 1.2$ (i)–(l); and $\mu = 2$(m)–(p) when a point source is placed at (0, 1.5 m). The horizontal and vertical coordinates of Poincare cross section are set as $X = x(1 + \frac{U_B^2}{\mu_B})$, $U = \frac{2}{\pi}\tan^{-1}(\frac{U_B^2}{\sqrt{\mu_B}})$. The square boxes of subgraphs are simulation areas, and the layered boundaries in the first two columns of subgraphs are perfect matching layers. The units of y-x coordinate axes are set as m. The duration of geometric trajectory is set as $\Delta t = 600$ ns.

Based on the refractive index $n(x, y)$ in Eq. (17), we set a simple model including NSEL and air background in Fig. 1(c). We set $\mu = 1$, 1.2, and 2 ($\mu_B = 1$, 0.8333 and 0.5), respectively, and incident a light beam from the left side or upper side of NSEL. The numerical results of geometrical optics and wave optics are shown in Figs. 5 and 6.

According to Fig. 5, when $\mu = 1$, the NSEL is equal to the traditional Eaton lens and leave NSEL 180° away from where it came in. When μ is greater than 1 (taking $\mu = 1.2$ as an example), the beam will diverge and most of the deflected angles will be greater than 180°. When μ continues to increase (taking $\mu = 2$ as an example), the deflected angle of the beam increases gradually and the ray begins to split sideways, resulting in strong scatterings in electric field. According to Eq. (16), $|dk_x/dt|$ has positive correlation with μ_B. When μ is greater than 1($\mu_B < 1$), $|dk_x/dt|$ of NSEL is smaller than $|dk_x/dt|$ of traditional Eaton lens. At the same time, $|dk_y/dt|$ does not change as much as $|dk_x/dt|$ when μ_B is changed.

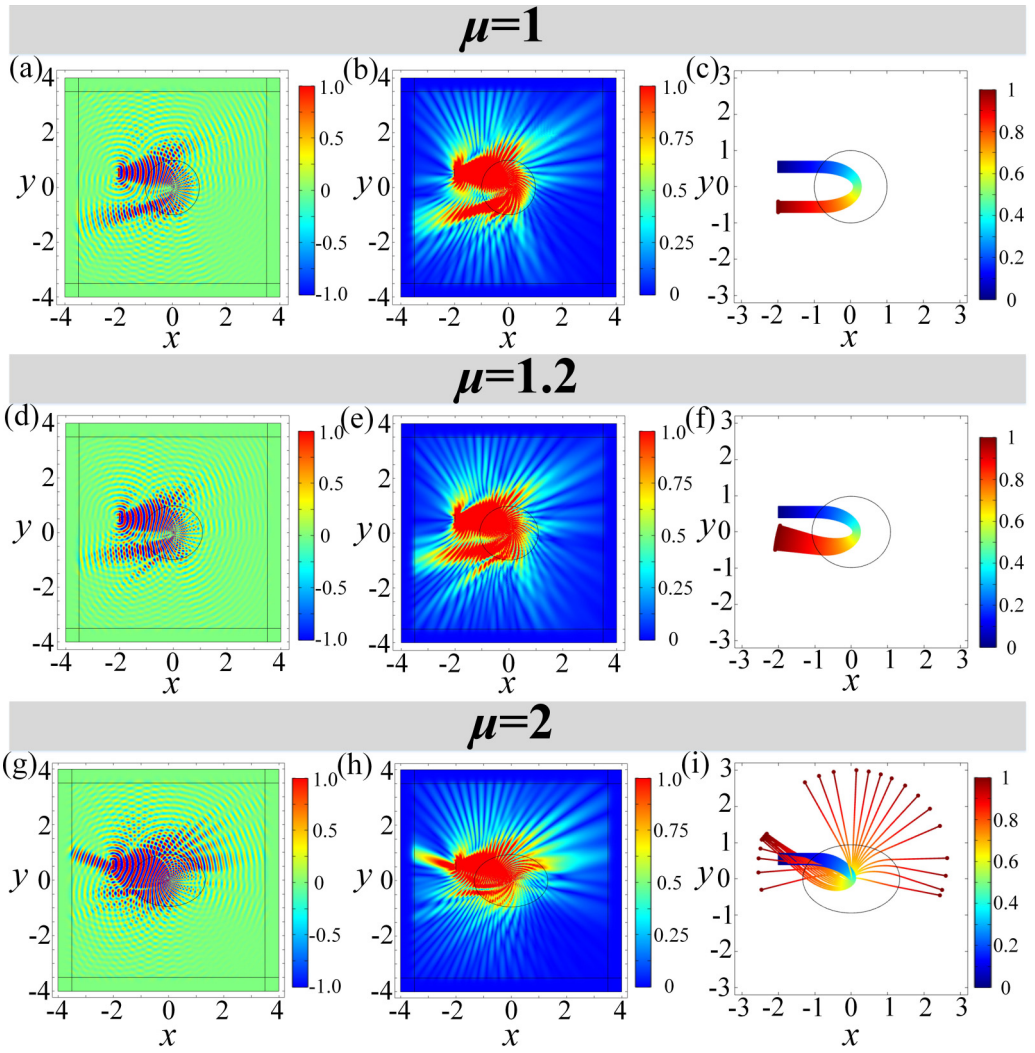

FIG. 5. The E_z component, absolute value of electric field and geometric trajectories with different mass ratios $\mu = 1$ (a)-(c), $\mu = 1.2$ (d)-(f) and $\mu = 2$ (g)-(i) when the beam is incident to the NSEL (the inner part of black circles in (a)-(c) or ellipse in (d)-(i) $\mu_B x_B^2 + y_B^2 = (\frac{2}{\mu_B^{-1/6}+1})^2$ in the center) from air background on the left side. The square boxes of subgraphs are simulation areas, and the layered boundaries in the first two columns of subgraphs are perfect matching layers. The units of y-x coordinate axes are set as m.

In other words, the change of k_x is less than that of k_y in the same time range. In traditional Eaton lens, between the time that beam passes through the x axis and leaves the lens, k_x decreases from zero to negative and k_y increases from negative to zero. Therefore in NSEL, k_y will increases from negative to positive when the beam leaves the lens. Hence, the ray keeps approaching the incident point as it leaves NSEL, as Figs. 5(d)–5(i) show.

In Fig. 6, when $\mu = 1$, in the same way, the beam will turn away 180° after passing through the lens. Between the time that the beam passes through the y axis and leaves the lens, k_x decreases from positive to zero and k_y increases from zero to positive. So when μ is greater than 1, k_y is still positive when the beam leaves the lens because the change of k_x is less than that of k_y in the same time range. Therefore, the beam keeps away from the incident point as it leaves NSEL, as Figs. 6(d)–6(i) show. In addition, the incident light beam will first converge (does not converge on a point) and then diverges after passing through the y axis with the deflected angle of less than 180° when μ is greater than 1. When μ continues to increases, the deflected angle decreases gradually and the convergence position is closer and closer to the origin. It is worth noting that there is not any scattering in other directions no matter what the value of μ is.

It is worth noting that the results are consistent except that the heavy axis and coordinate axis are swapped over when μ is replaced with $1/\mu$, which is because μ_B will be the same mass factor on the new heavy axis (y axis) after coordinate transformation.

IV. CONCLUSION

In this paper, it is proved that AKP in two-body motion has similar properties to the NSEL under certain conditions. Therefore, we reproduce the mechanical behavior of AKP from the perspective of wave optics and geometric optics by studying the electric field and ray trajectories with different mass ratios μ. The results show that with the increase of μ, the self-focusing property of the traditional Eaton lens will be lost, and when the point source is placed on the left side

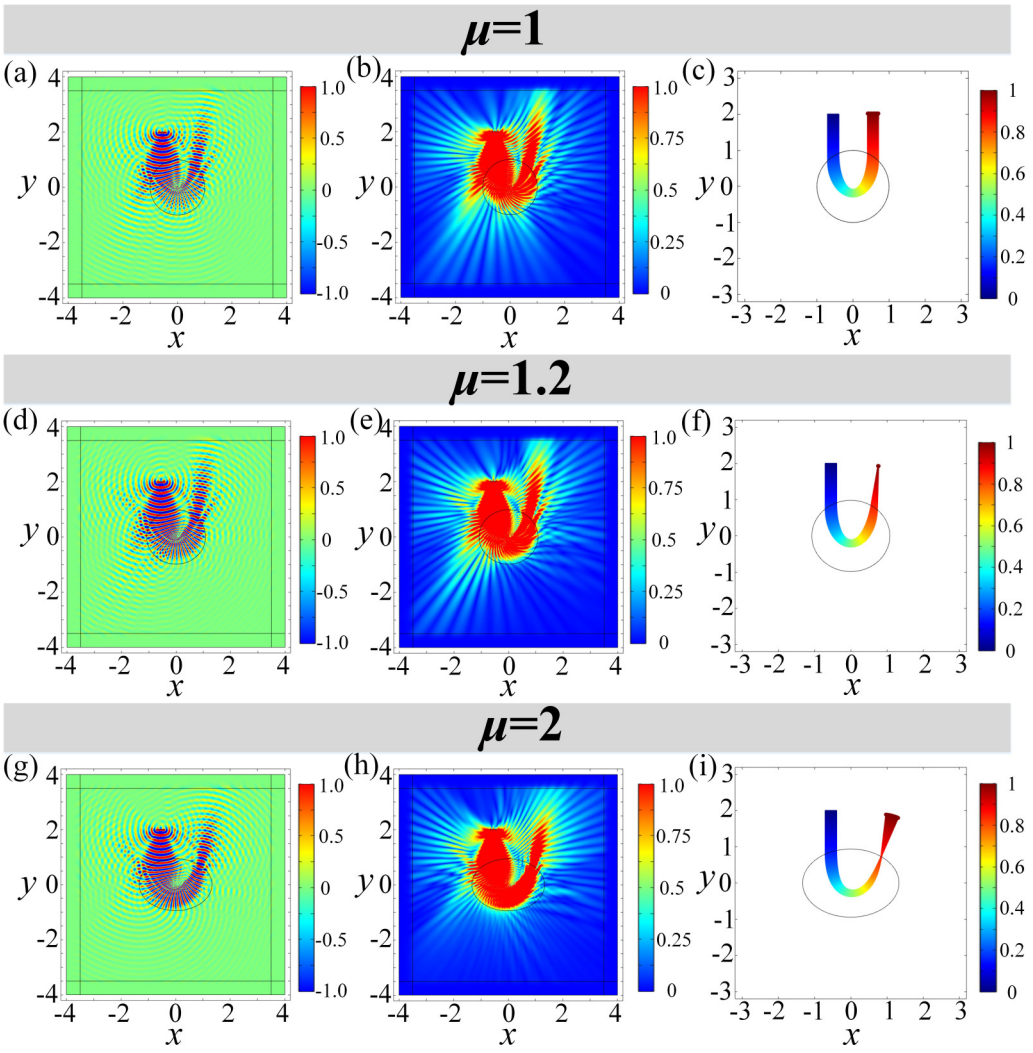

FIG. 6. The E_z component, absolute value of electric field and geometric trajectories with different mass ratios $\mu = 1$ (a)-(c), $\mu = 1.2$ (d)-(f) and $\mu = 2$ (g)-(i) when the beam is incident to the NSEL (the inner part of black circles in (a)-(c) or ellipse in (d)-(i) $\mu_B x_B^2 + y_B^2 = (\frac{2}{\mu_B^{-1/6}+1})^2$ in the center) from air background on the upper side. The square boxes of subgraphs are simulation areas, and the layered boundaries in the first two columns of subgraphs are perfect matching layers. The units of y-x coordinate axes are set as m.

or upper side, the electric field and ray will change from elliptic (periodic orbit) to quasiperiodic orbits of symmetric irregular shape, and finally to chaotic distribution. According to Poincaré cross section, we can also observe the evolution from solitary points to closed curves and then to dense points, which is very similar to the phenomena of AKP. When a beam is incident to NSEL from air, the deflected angle of the beam from the left side is greater than 180° and increases gradually, causing strong scattering, which is consistent with chaos states, while the deflected angle of the beam from the upper side is less than 180° and becomes smaller and smaller with the increase of μ. Based on this correspondence between AKP and NSEL, more related applications such as superscattering and new light field regulations, will be achieved by combining some transformation optics principles [13,14,32,33] in the future.

ACKNOWLEDGMENTS

This work is supported by the National Natural Science Foundation of China (Grants No. 92050102 and No. 11874311), the National Key Research and Development Program of China (Grant No. 2020YFA0710100), and the Fundamental Research Funds for the Central Universities (Grant No. 20720200074).

[1] M. C. Gutzwiller, The anisotropic Kepler problem in two dimensions, J. Math. Phys. **14**, 139 (1973).
[2] M. C. Gutzwiller, Bernoulli sequences and trajectories in the anisotropic Kepler problem, J. Math. Phys. **18**, 806 (1977).
[3] R. Broucke, *Dynamical Astronomy* (University of Texas Press, Austin, Texas, 1985), p. 9.
[4] M. C. Gutzwiller, *Chaos in Classical and Quantum Mechanics* (Springer Press, New York, 1990), p. 156.

[5] Z. Q. Bai and W. M. Zheng, Singularity in classical and quantum Kepler problem with weak anisotropy, Phys. Lett. A **300**, 259 (2002).
[6] G. Contopoulos and M. Harsoula, Stability and instability in the anisotropic Kepler problem, J. Phys. A: Gen. Phys. **38**, 8897 (2005).
[7] M. Arribas, A. Elipe, and A. Riaguas, Non-integrability of anisotropic quasihomogeneous Hamiltonian systems, Mech. Res. Commun. **30**, 209 (2003).
[8] E. I. Abouelmagd, J. Llibre, and J. Guirao, Periodic orbits of the planar anisotropic Kepler problem, Int. J. Bifurcat. Chaos **27**, 1750039 (2017).
[9] R. L. Devaney, Triple collision in the planar isosceles three-body problem, Invent. Math. **60**, 249 (1980).
[10] R. L. Devaney, Blowing up singularities in classical mechanical systems, Am. Math. Mon. **89**, 535 (1982).
[11] J. Delgado, E. A. Lacomba, E. Pérez-Chavela, and J. Llibre, *Hamiltonian Systems and Celestial Mechanics* (World Scientific Press, Singapore, 2000), p. 1.
[12] S. Zhang, D. A. Genov, C. Sun, and X. Zhang, Cloaking of Matter Waves, Phys. Rev. Lett. **100**, 123002 (2008).
[13] J. B. Pendry, D. Schurig, and D. R. Smith, Controlling electromagnetic fields, Science **312**, 1780 (2006).
[14] H. Chen, U. Leonhardt, and T. Tyc, Conformal cloak for waves, Phys. Rev. A **83**, 055801 (2011).
[15] A. J. Maciejewski, M. Przybylska, and S. Wojciech, Anisotropic Kepler and anisotropic two fixed centres problems, Celest. Mech. Dyn. Astron. **127**, 163 (2016).
[16] J. L. Synge, The absolute optical instrument, Trans. Am. Math. Soc. **44**, 32 (1938).
[17] M. Born and E. Wolf, *Principles of Optics* (Cambridge University Press, Cambridge, England, 2006).
[18] T. Tyc, L. Herzánová, M. Šarbort, and K. Bering, Absolute instruments and perfect imaging in geometrical optics, New J. Phys. **13**, 115004 (2011).
[19] L. Xu and H. Chen, Conformal transformation optics, Nat. Photonics **9**, 15 (2015).
[20] J. C. Miñano, Perfect imaging in a homogeneous three dimensional region, Opt. Express **14**, 9627 (2006).
[21] R. K. Luneburg, *Mathematical Theory of Optics* (University of California Press, Berkeley, 1964).
[22] J. Eaton, On spherically symmetric lenses, Trans. IRE Antennas Propag. **PGAP-4**, 66 (1952).
[23] Y. G. Ma, C. K. Ong, T. Tyc, and U. Leonhardt, An omnidirectional retroreflector based on the transmutation of dielectric singularities, Nat. Mater. **8**, 639 (2009).
[24] J. C. Maxwell, Problems(3), Camb. Dublin Math. J. **8**, 188 (1854).
[25] J. C. Maxwell, On the general laws of optical instruments, Q. J. Pure Appl. Math. **2**, 233 (1858).
[26] A. J. Danner, H. L. Dao, and T. Tyc, The Lissajous lens: A three-dimensional absolute optical instrument without spherical symmetry, Opt. Express **23**, 5716 (2015).
[27] H. Peng, H. Han, P. He, K. Xia, J. Zhang, X. Li, Q. Bao, Y. Chen, and H. Chen, The Luneburg-Lissajous lens, EPL (Europhysics Letters) **129**, 64001 (2020).
[28] V. N. Smolyaninova, I. I. Smolyaninov, A. V. Kildishev, and V. M. Shalaev, Maxwell fish-eye and Eaton lenses emulated by microdroplets, Opt. Lett. **35**, 3396 (2010).
[29] M. R. Forouzeshfard and T. Tyc, Photonic crystals composed of Eaton lenses and invisible lenses, Phys. Rev. A **95**, 013822 (2017).
[30] M. Šarbort and T. Tyc, Spherical media and geodesic lenses in geometrical optics, J. Optics-UK **14**, 075705 (2012).
[31] L. Xu, T. Tyc, and H. Chen, Conformal optical devices based on geodesic lenses, Opt. Express **27**, 28722 (2019).
[32] M. M. Sadeghi, S. Li, L. Xu, B. Hou, and H. Chen, Transformation optics with Fabry-Pérot resonances, Sci. Rep-UK. **5**, 8680 (2015).
[33] P. F. Zhao, G. X. Cai, and H. Chen, Exact transformation optics by using electrostatics, Sci. Bull. **67**, 246 (2022).